ACADEMIC PRESS

Available online at www.sciencedirect.com

SCIENCE DIRECT®

Journal of Computational Physics 186 (2003) 666–689

JOURNAL OF COMPUTATIONAL PHYSICS

www.elsevier.com/locate/jcp

Interpolating wavelet collocation method of time dependent Maxwell's equations: characterization of electrically large optical waveguide discontinuities

Masafumi Fujii [a,*], Wolfgang J.R. Hoefer [b]

[a] *Institute for High Frequency Technique, Technical University of Munich, Arcisstrasse 21, Munich D-80333, Germany*
[b] *Department of Electrical and Computer Engineering, University of Victoria, Victoria, BC, Canada V8W 3P6*

Received 13 August 2001; accepted 27 March 2002

Abstract

Biorthogonal interpolating wavelets have been applied to electromagnetic field modeling through the wavelet collocation method in time domain, yielding a versatile first-principle algorithm for the solution of time dependent Maxwell's equations with inhomogeneous media. The resulting scheme maintains high accuracy, while, by virtue of its sub-gridding capability, significant reduction of the computational expenditure has been obtained. The proposed method has been applied to the analysis of two-dimensional dielectric waveguide discontinuities. Particularly for the modeling of electrically large optical waveguides, where the dimension of the analyzed structure is much larger than the wavelength of the highest frequency content of the transmitted signal, the proposed method has been proven to be highly efficient compared to the standard finite-difference method.

Keywords: Time domain electromagnetic field analysis; Inhomogeneous media; Biorthogonal interpolating wavelets; Wavelet collocation technique

1. Introduction

Wavelets have been widely investigated to improve the efficiency in solving partial differential equations (PDEs). In the previously reported methods [6,10], differentials or multiplication operators are represented in the wavelet bases such as Daubechies compactly supported wavelets [8], and the equations are solved in the space of wavelet coefficients. The formulations are basically derived through the wavelet-Galerkin method [4,25], or through the wavelet-collocation method [1,19]. In these methods, the PDEs are reduced to a system of algebraic equations with small numbers of unknowns after the coefficients smaller than a certain

* Corresponding author.
E-mail address: fujii@ei.tum.de (M. Fujii).

0021-9991/03/$ - see front matter
doi:10.1016/S0021-9991(03)00091-3

threshold are ignored, leading to an efficient numerical algorithm of reduced computational cost compared to, e.g., the finite-difference methods and the finite-element methods.

It has been reported in [21] that the autocorrelation function of the Daubechies compactly supported scaling functions are effectively used in a wavelet-Galerkin method as an interpolation basis to solve elliptic equations. The interpolation basis is also obtained by the interpolation subdivision scheme of Deslauriers and Dubuc [7,23]. In [16], the sparse point representation has been proposed, which is a scheme based on an interpolating wavelet transform using polynomial interpolation on dyadic grids. The major advantage of employing the interpolating wavelets as bases is that the expansion coefficients to the scaling functions are the direct sampled values of the physical quantities, hence the interpolating basis serves to avoid the reconstruction of the total values. This feature is particularly suitable for the solution of PDEs for multi-dimensional problems, resulting in a significant reduction of computational cost compared to the non-interpolating bases. It has been shown in [18] that the incorporation of the second-generation wavelets recently developed by Sweldens [26] overcomes some of the shortcomings existed in the wavelet-collocation method.

Above-mentioned methods have mostly been applied to one-space-dimensional fluid dynamics problems such as the advection equations and Burgers equations. Apart from the fluid dynamics, electromagnetic field analysis, i.e., the solution of Maxwell's equations by using wavelets has also been extensively investigated. They are a system of partial differential equations of hyperbolic type consisting of first-order derivatives in time and in space. In [17], the Battle–Lemarié wavelets have been applied to the solution of the time-dependent Maxwell's equations in the context of the wavelet-Galerkin method; the space discretization is given in the wavelet coefficient domain, and the time marching is performed by the standard explicit finite-difference scheme. This method is similar to the higher-order finite-difference time-domain (FDTD) method [9] and has highly linear numerical dispersion characteristics, yielding an accurate numerical solution and reduced computational expenditure with coarser discretization. The shifted interpolation property of the Daubechies compactly supported scaling functions [27] has been applied in [28] as in the same context of [17]. Since the basis function is interpolating, the scaling function coefficients are the direct physical sampled values, one can obtain a simple and versatile numerical algorithm.

The authors have investigated the numerical dispersion errors of those methods and have extended them by using the Daubechies scaling functions of higher regularity in [12]; however, only the scaling function was used because the wavelets do not have the interpolation property. It has been shown in [14] that the extended method is advantageous in analyzing electrically large inhomogeneous structures such as optical waveguides, where the scale of the object is much larger than the wavelength of the highest frequency content of the transmitted signal.

The authors then applied the biorthogonal interpolating wavelets [2,26] to the solution of Maxwell's equations in a homogeneous medium in the context of the wavelet-collocation method; the Deslauriers–Dubuc interpolating functions [7,23] are adopted as the scaling functions, and their shifted and contracted versions as the wavelets. This has been briefly reported in the authors' letter paper [13] for an homogeneous medium in the two-dimensional settings. These basis functions constitute non-L^2 biorthogonal bases that are smooth, symmetric, compactly supported and exactly interpolating. Unlike the Daubechies orthogonal wavelets, of which interpolation property is limited to the bases of low regularity, the proposed basis set yields a scheme of desired order of regularity as well as saves the computational overhead of total field reconstruction.

This paper describes the method in [13] in more detail, and extends the formulation in particular to the analysis of general inhomogeneous dielectric media; it is shown that a simple and versatile algorithm is given by using the interpolating wavelet basis. The numerical dispersion error is then investigated in detail to clarify the accuracy of the method, and the results are compared to those of the higher-order finite-difference schemes. Verification is also made by the analysis of square resonators. The proposed method is finally applied to the analysis of two-dimensional dielectric waveguide structures that have the typical size

of optical waveguides. By applying wavelets only where higher resolution is desired as decided a priori, the proposed method provides a sub-gridding capability. Although the ultimate goal of the wavelet-based method is an efficient adaptive gridding, this paper demonstrate that significant reduction of the computational cost can be achieved with the sub-gridding technique for the typical optical waveguide problems.

The optical waveguide in the current high-speed data communication system has a very large-scaled structure compared to the wavelength of the transmitted signal, so-called the electrically large structure. There exist various numerical methods proposed in literature. However, the optical waveguides including discontinuities are difficult to analyze due to the excessive computational requirement; e.g., since the standard FDTD method requires discretization of one twentieth wavelength for suitably accurate analysis, a friction of optical waveguide as short as 10 μm having a 5×5 μm^2 cross section with the refractive index 3 needs the discretization of 0.025 μm per dimension, resulting in as many as $400 \times 200 \times 200$ cells; it will be necessary to use a supercomputers or a high-end workstation with extensive memory for the analysis of those structures. Although optical waveguides are typically analyzed with the various modified versions of the beam propagation method (BPM) [3,11], it is difficult to be applied to the waveguide discontinuities since it is a discretization of the wave equation and the reflection of waves is intrinsically not taken into consideration. To the best of the authors' knowledge, practically no efficient numerical technique exists for the accurate analysis of general optical waveguide discontinuities. This paper proposes an efficient algorithm that allows the analysis of electrically large optical waveguides with inhomogeneous discontinuities within a limited computational resource.

2. Formulation

2.1. Interpolating wavelet basis

The Deslauriers–Dubuc interpolating function ϕ of order $2p-1$ is given by an autocorrelation function of the Daubechies compactly supported orthogonal scaling functions ϕ_0 of p vanishing wavelet moments [24] as

$$\phi(x) = \int_{-\infty}^{+\infty} \phi_0(u)\phi_0(u-x)\,\mathrm{d}u, \tag{1}$$

which has even-symmetry and minimum support of $[-2p+1, 2p-1]$ as shown in Fig. 1 for $p = 2, 4$ and 10, and reproduces polynomials of order $2p-1$.

We adopt ϕ as a scaling function, which satisfies the so-called dilation relation [24]

$$\phi(x) = \sum_{k=-\infty}^{+\infty} h_k^* \phi(2t-k), \tag{2}$$

where the filter coefficient h_k^* is determined by the convolution of the filter of the Daubechies compactly supported wavelets of p-vanishing moments h_k [8] as

$$h_k^* = \sum_{m=-\infty}^{+\infty} h_m h_{m-k}, \tag{3}$$

which is listed for $p = 2$, 4 and 10 in Table 1. It can be shown that $h^*_{-k} = h_k^*$ holds.Then, the wavelet function which creates the 'detail' space can be chosen as

$$\psi(x) = \phi(2x-1). \tag{4}$$

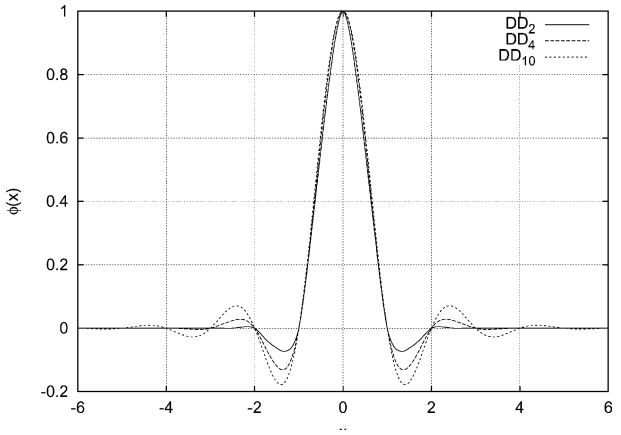

Fig. 1. Deslauriers–Dubuc interpolating function DD_p of order $2p-1$ for $p=2$, 4 and 10.

Table 1
Filter coefficients h_k^* for the Deslauriers–Dubuc interpolating function DD_p with $p=2$, 4 and 10

k	$p=2$	$p=4$	$p=10$
0	1.0	1.0	1.0
1	0.56250000	0.59814453	0.62090802
2	0.0	0.0	0.0
3	−0.06250000	−0.11962891	−0.16933855
4		0.0	0.0
5		0.02392578	0.06773542
6		0.0	0.0
7		−0.00244141	−0.02605208
8			0.0
9			0.00868403
10			0.0
11			−0.00236837
12			0.0
13			0.00050100
14			0.0
15			−0.00007662
16			0.0
17			0.00000751
18			0.0
19			−0.00000035

$h_{-k}^* = h_k^*$.

Although (4) is not a true wavelet since it has no vanishing moment, it generates multiresolution analysis and plays the same role as other wavelets in the context of the wavelet-collocation method. In order to form a biorthogonal basis, the dual scaling and wavelet functions are chosen to be the Dirac delta function and a linear combination of Diracs, respectively, as

$$\tilde{\phi}(x) = \delta(x), \tag{5}$$

$$\tilde{\psi}(x) = \sum_{k=-2p+2}^{2p} (-1)^{k-1} h_{-k+1}^* \delta\left(x - \frac{k}{2}\right). \tag{6}$$

Since the Dirac delta is not in the space of square integrable functions, the resulting basis set is in non-L^2 space. Let

$$f_j(x) = f((x/\Delta x) - j) \tag{7}$$

for $f = \phi, \psi, \tilde{\phi}$ and $\tilde{\psi}$ and j integer with Δx being the spatial discretization interval, then the set of the basis functions satisfies the biorthogonal relations

$$\left\langle \phi_i | \tilde{\phi}_j \right\rangle = \delta_{ij}, \tag{8}$$

$$\left\langle \psi_i | \tilde{\psi}_j \right\rangle = \delta_{ij}, \tag{9}$$

$$\left\langle \phi_i | \tilde{\psi}_j \right\rangle = \left\langle \psi_i | \tilde{\phi}_j \right\rangle = 0, \tag{10}$$

where $\langle \cdot | \cdot \rangle$ denotes the inner product of the functions and δ_{ij} the Kronecker delta function.

2.2. Discretization of Maxwell's equations

We consider Maxwell's curl equations in the Cartesian coordinate system for inhomogeneous isotropic lossy media in the 2D TE-polarized case, where the wave of electric field E_y and magnetic field H_x and H_z propagates in the xz-plane,

$$-\mu \frac{\partial H_x}{\partial t} = -\frac{\partial E_y}{\partial z}, \tag{11}$$

$$-\mu \frac{\partial H_z}{\partial t} = \frac{\partial E_y}{\partial x}, \tag{12}$$

$$J_y + \sigma \frac{D_y}{\varepsilon} + \frac{\partial D_y}{\partial t} = \frac{\partial H_x}{\partial z} - \frac{\partial H_z}{\partial x}, \tag{13}$$

where J_y is the source current density, ε the dielectric permittivity, and σ the electric conductivity of the media. In order to take into account the inhomogeneity of the media we consider the constitutive equation for the electric flux density D_y and the electric field E_y

$$D_y = \varepsilon E_y. \tag{14}$$

Here we introduce a rectangular pulse function

$$h(t) = \begin{cases} 1 & \text{for } 0 < t < 1, \\ 1/2 & \text{for } t = 0, 1, \\ 0 & \text{elsewhere}, \end{cases} \tag{15}$$

and its discrete form

$$h_n(t) = h\left(\frac{t}{\Delta t} - n + \frac{1}{2} \right), \tag{16}$$

for n integer and Δt being the time step. The electromagnetic field variables are then expanded in the scaling function ϕ_i and the wavelet function ψ_i in space and in the rectangular pulse function h_n in time, with i and n integer,

$$E_y(x,z,t) = \sum_{i,k,n=-\infty}^{+\infty} \{E^{y,\phi\phi}_{i,k,n+1/2}\,\phi_i(x)\,\phi_k(z) + E^{y,\phi\psi}_{i,k+1/2,n+1/2}\,\phi_i(x)\,\psi_k(z) + E^{y,\psi\phi}_{i+1/2,k,n+1/2}\,\psi_i(x)\,\phi_k(z) + E^{y,\psi\psi}_{i+1/2,k+1/2,n+1/2}\,\psi_i(x)\,\psi_k(z)\}\,h_{n+1/2}(t), \tag{17}$$

$$D_y(x,z,t) = \sum_{i,k,n=-\infty}^{+\infty} \{D^{y,\phi\phi}_{i,k,n+1/2}\,\phi_i(x)\,\phi_k(z) + D^{y,\phi\psi}_{i,k+1/2,n+1/2}\,\phi_i(x)\,\psi_k(z) + D^{y,\psi\phi}_{i+1/2,k,n+1/2}\,\psi_i(x)\,\phi_k(z) + D^{y,\psi\psi}_{i+1/2,k+1/2,n+1/2}\,\psi_i(x)\,\psi_k(z)\}\,h_{n+1/2}(t), \tag{18}$$

$$H_x(x,z,t) = \sum_{i,k,n=-\infty}^{+\infty} \{H^{y,\phi\phi}_{i,k+1/2,n}\,\phi_i(x)\,\phi_{k+1/2}(z) + H^{y,\phi\psi}_{i,k+1,n}\,\phi_i(x)\,\psi_{k+1/2}(z) + H^{y,\psi\phi}_{i+1/2,k+1/2,n}\,\psi_i(x)\,\phi_{k+1/2}(z) + H^{y,\psi\psi}_{i+1/2,k+1,n}\,\psi_i(x)\,\psi_{k+1/2}(z)\}\,h_n(t), \tag{19}$$

$$H_z(x,z,t) = \sum_{i,k,n=-\infty}^{+\infty} \{H^{z,\phi\phi}_{i+1/2,k,n}\,\phi_{i+1/2}(x)\,\phi_k(z) + H^{z,\phi\psi}_{i+1/2,k+1/2,n}\,\phi_{i+1/2}(x)\,\psi_k(z) + H^{z,\psi\phi}_{i+1,k,n}\,\psi_{i+1/2}(x)\,\phi_k(z) + H^{z,\psi\psi}_{i+1,k+1/2,n}\,\psi_{i+1/2}(x)\,\psi_k(z)\}\,h_n(t). \tag{20}$$

The expansion coefficients for the wavelet terms are defined on the Yee cell [9], as shown in Fig. 2, at nodes halfway between the regular nodes in the direction of the corresponding wavelets.

The derivation of the time evolution equations through the wavelet collocation procedure is similar to that of [17,20]. However, the use of the biorthogonal interpolets associated with the duals in the form of the Dirac delta functions significantly simplifies the treatment of inhomogeneous media.

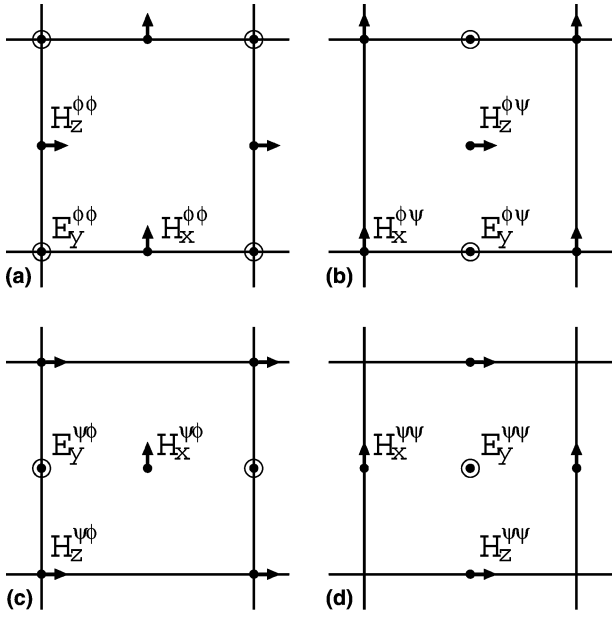

Fig. 2. Definition of the node points for the basis functions: (a) $\phi(x)\phi(z)$, (b) $\phi(x)\psi(z)$, (c) $\psi(x)\phi(z)$, and (d) $\psi(x)\psi(z)$.

Now we discretize the governing equations; suppose ε is inhomogeneous in space, we first discretize the constitutive Eq. (14) by taking inner products between each side of (14) and the testing function $\tilde{\phi}_{i'}\tilde{\phi}_{k'}h_{n'+1/2}$ for the scaling function coefficients

$$\left\langle D_y(x,z,t)|\tilde{\phi}_{i'}\tilde{\phi}_{k'}h_{n'+1/2}\right\rangle = \left\langle \varepsilon(x,z)E_y(x,z,t)|\tilde{\phi}_{i'}\tilde{\phi}_{k'}h_{n'+1/2}\right\rangle. \tag{21}$$

Substituting the field expansions (17) and (18) to (21) and taking into consideration the biorthogonality relation (8), the left-hand side of (21) leads to

$$\begin{aligned}\int\int\int D_y(x,z,t)\tilde{\phi}_{i'}(x)\tilde{\phi}_{k'}(z)h_{n'+1/2}(t)\,\mathrm{d}x\,\mathrm{d}z\,\mathrm{d}t &= \sum_{i,k,n=-\infty}^{+\infty} D^{y,\phi\phi}_{i,k,n+1/2}\delta_{ii'}\delta_{kk'}\delta_{nn'}\,\Delta x\,\Delta z\,\Delta t \\ &= D^{y,\phi\phi}_{i',k',n'+1/2}\,\Delta x\,\Delta z\,\Delta t,\end{aligned} \tag{22}$$

and the right-hand side of (21) leads to

$$\begin{aligned}&\int\int\int \varepsilon(x,z)E_y(x,z,t)\tilde{\phi}_{i'}(x)\tilde{\phi}_{k'}(z)h_{n'+1/2}(t)\,\mathrm{d}x\,\mathrm{d}z\,\mathrm{d}t \\ &= \sum_{i,k=-\infty}^{+\infty} E^{y,\phi\phi}_{i,k,n'+1/2}\int\int \phi_i(x)\phi_k(z)\varepsilon(x,z)\tilde{\phi}_{i'}(x)\tilde{\phi}_{k'}(z)\,\mathrm{d}x\,\mathrm{d}z\,\Delta t \\ &\quad + \sum_{i,k=-\infty}^{+\infty} E^{y,\phi\psi}_{i,k,n'+1/2}\int\int \phi_i(x)\psi_k(z)\varepsilon(x,z)\tilde{\phi}_{i'}(x)\tilde{\phi}_{k'}(z)\,\mathrm{d}x\,\mathrm{d}z\,\Delta t \\ &\quad + \sum_{i,k=-\infty}^{+\infty} E^{y,\psi\phi}_{i,k,n'+1/2}\int\int \psi_i(x)\phi_k(z)\varepsilon(x,z)\tilde{\phi}_{i'}(x)\tilde{\phi}_{k'}(z)\,\mathrm{d}x\,\mathrm{d}z\,\Delta t \\ &\quad + \sum_{i,k=-\infty}^{+\infty} E^{y,\psi\psi}_{i,k,n'+1/2}\int\int \psi_i(x)\psi_k(z)\varepsilon(x,z)\tilde{\phi}_{i'}(x)\tilde{\phi}_{k'}(z)\,\mathrm{d}x\,\mathrm{d}z\,\Delta t \\ &= \sum_{i,k=-\infty}^{+\infty} E^{y,\phi\phi}_{i,k,n'+1/2}\varepsilon(i'\Delta x,k'\Delta z)\delta_{ii'}\delta_{kk'}\,\Delta x\,\Delta z\,\Delta t \qquad (23)\\ &= E^{y,\phi\phi}_{i',k',n'+1/2}\varepsilon(i'\Delta x,k'\Delta z)\,\Delta x\,\Delta z\,\Delta t. \qquad (24)\end{aligned}$$

Note that although (23) consists of ε-weighted inner products, the last three terms in (23) vanish thanks to the dual functions in the form of the Dirac delta function. From (22) and (24) we obtain the local relation between the scaling function coefficients of E_y and D_y as

$$D^{y,\phi\phi}_{i,k,n+1/2} = \varepsilon_{i,k}E^{y,\phi\phi}_{i,k,n+1/2}, \tag{25}$$

where $\varepsilon_{i,k}$ denotes the local dielectric permittivity defined by

$$\varepsilon_{i,k} \equiv \varepsilon(i\Delta x,k\Delta z). \tag{26}$$

To obtain the wavelet coefficients of E_y and D_y, we test (14) with the dual basis function $\tilde{\phi}_{i'}\tilde{\psi}_{k'}h_{n'+1/2}$ as

$$\left\langle D_y(x,z,t)|\tilde{\phi}_{i'}\tilde{\psi}_{k'}h_{n'+1/2}\right\rangle = \left\langle \varepsilon(x,z)E_y(x,z,t)|\tilde{\phi}_{i'}\tilde{\psi}_{k'}h_{n'+1/2}\right\rangle. \tag{27}$$

Similarly as for the scaling function coefficients, substituting the field expansions to (27), the left-hand side of (27) leads to

$$\int\int\int D_y(x,z,t)\tilde{\phi}_{i'}(x)\tilde{\psi}_{k'}(z)h_{n'+1/2}(t)\,\mathrm{d}x\,\mathrm{d}z\,\mathrm{d}t = \sum_{i,k,n=-\infty}^{+\infty} D^{y,\phi\psi}_{i,k,n+1/2}\delta_{ii'}\delta_{kk'}\delta_{nn'}\,\Delta x\,\Delta z\,\Delta t$$
$$= D^{y,\phi\psi}_{i',k',n'+1/2}\,\Delta x\,\Delta z\,\Delta t, \tag{28}$$

and the right-hand side of (27) leads to

$$\begin{aligned}
&\int\int\int \varepsilon(x,z)E_y(x,z,t)\tilde{\phi}_{i'}(x)\tilde{\psi}_{k'}(z)h_{n'+1/2}(t)\,\mathrm{d}x\,\mathrm{d}z\,\mathrm{d}t\\
&= \sum_{i,k=-\infty}^{+\infty} E^{y,\phi\phi}_{i,k,n'+1/2}\int\int \phi_i(x)\phi_k(z)\varepsilon(x,z)\tilde{\phi}_{i'}(x)\tilde{\psi}_{k'}(z)\,\mathrm{d}x\,\mathrm{d}z\,\Delta t\\
&\quad+\sum_{i,k=-\infty}^{+\infty} E^{y,\phi\psi}_{i,k,n'+1/2}\int\int \phi_i(x)\psi_k(z)\varepsilon(x,z)\tilde{\phi}_{i'}(x)\tilde{\psi}_{k'}(z)\,\mathrm{d}x\,\mathrm{d}z\,\Delta t\\
&\quad+\sum_{i,k=-\infty}^{+\infty} E^{y,\psi\phi}_{i,k,n'+1/2}\int\int \psi_i(x)\phi_k(z)\varepsilon(x,z)\tilde{\phi}_{i'}(x)\tilde{\psi}_{k'}(z)\,\mathrm{d}x\,\mathrm{d}z\,\Delta t\\
&\quad+\sum_{i,k=-\infty}^{+\infty} E^{y,\psi\psi}_{i,k,n'+1/2}\int\int \psi_i(x)\psi_k(z)\varepsilon(x,z)\tilde{\phi}_{i'}(x)\tilde{\psi}_{k'}(z)\,\mathrm{d}x\,\mathrm{d}z\,\Delta t, \qquad (29)\\
&= \sum_{k=-\infty}^{+\infty} E^{y,\phi\phi}_{i',k,n'+1/2}\int \phi_k(z)\varepsilon(i'\Delta x,z)\tilde{\psi}_{k'}(z)\,\mathrm{d}z\,\Delta x\,\Delta t\\
&\quad+\sum_{i,k=-\infty}^{+\infty} E^{y,\phi\psi}_{i,k,n'+1/2}\varepsilon(i'\Delta x,k'\Delta z)\delta_{ii'}\delta_{kk'}\,\Delta x\,\Delta z\,\Delta t\\
&= \sum_l \eta^{\phi\psi}_{i,k}(l)E^{y,\phi\phi}_{i',k'+l,n'+1/2}\,\Delta x\,\Delta z\,\Delta t\\
&\quad+E^{y,\phi\psi}_{i',k',n'+1/2}\varepsilon(i'\Delta x,k'\Delta z)\,\Delta x\,\Delta z\,\Delta t, \qquad (30)
\end{aligned}$$

where the ε-weighted connection coefficient $\eta^{\phi\psi}_{i,k}(l)$ is defined by

$$\left\langle \phi_k(z)\varepsilon(i\Delta x,z)\middle|\tilde{\psi}_{k'}(z)\right\rangle \equiv \sum_l \eta^{\phi\psi}_{i,k}(l)\delta_{k,k'+l}\Delta z, \tag{31}$$

and is reduced to a simple expression using the filter coefficients h^*_k of (3) as

$$\begin{aligned}
\eta^{\phi\psi}_{i,k}(l) &\equiv \frac{1}{\Delta z}\left\langle \phi_k(z)\varepsilon(i\Delta x,z)\middle|\tilde{\psi}_{k-l}(z)\right\rangle\\
&= \sum_{m=-2p+2}^{2p}(-1)^{m+1}h^*_{-m+1}h^*_{-2l+m}\varepsilon_{i,k-l+m/2} = h^*_{-2l+1}(\varepsilon_{i,k-l+1/2}-\varepsilon_{i,k}).
\end{aligned} \tag{32}$$

In (29), the last two terms vanish and two remain. From (27), (30) and (32) the constitutive relation of the wavelet coefficients is given by

$$D^{y,\phi\psi}_{i,k+1/2,n+1/2} = \sum_l \eta^{\phi\psi}_{i,k}(l)E^{y,\phi\phi}_{i,k+l,n+1/2} + \varepsilon_{i,k+1/2}E^{y,\phi\psi}_{i,k+1/2,n+1/2}. \tag{33}$$

As in the similar manner, the relations between the rest of the wavelet coefficients are given by

$$D^{y,\psi\phi}_{i+1/2,k,n+1/2} = \sum_l \eta^{\psi\phi}_{i,k}(l)E^{y,\phi\phi}_{i+l,k,n+1/2} + \varepsilon_{i+1/2,k}E^{y,\psi\phi}_{i+1/2,k,n+1/2}, \tag{34}$$

$$D^{y,\psi\psi}_{i+1/2,k+1/2,n+1/2} = \sum_l \sum_m \eta^{\psi\psi}_{i,k}(l,m) E^{y,\phi\phi}_{i+l,k+m,n+1/2} + \sum_l \eta^{\psi\psi}_{i,k+1/2}(l) E^{y,\phi\psi}_{i+l,k+1/2,n+1/2} + \sum_m \eta^{\psi\psi}_{i+1/2,k}(m) E^{y,\psi\phi}_{i+1/2,k+m,n+1/2} + \varepsilon_{i+1/2,k+1/2} E^{y,\psi\psi}_{i+1/2,k+1/2,n+1/2}. \tag{35}$$

For (34), the coefficient $\eta^{\psi\phi}_{i,k}(l)$ is given by

$$\eta^{\psi\phi}_{i,k}(l) \equiv \frac{1}{\Delta x}\left\langle \phi_i(x)\varepsilon(x,k\Delta z)\middle|\tilde{\psi}_{i-l}(x)\right\rangle = h^*_{-2l+1}(\varepsilon_{i-l+1/2,k} - \varepsilon_{i,k}), \tag{36}$$

and for (35),

$$\eta^{\psi\psi}_{i,k}(l,m) \equiv \frac{1}{\Delta x\Delta z}\left\langle \phi_i(x)\phi_k(z)\varepsilon(x,z)\middle|\tilde{\psi}_{i-l}(x)\tilde{\psi}_{k-m}(z)\right\rangle = h^*_{-2l+1}h^*_{-2m+1}(\varepsilon_{i-l+1/2,k-m+1/2} - \varepsilon_{i-l+1/2,k} - \varepsilon_{i,k-m+1/2} + \varepsilon_{i,k}), \tag{37}$$

$$\eta^{\psi\psi}_{i,k+1/2}(l) \equiv \frac{1}{\Delta x}\left\langle \phi_i(x)\varepsilon(x,k\Delta z)\middle|\tilde{\psi}_{i-l}(x)\right\rangle = h^*_{-2l+1}(\varepsilon_{i-l+1/2,k+1/2} - \varepsilon_{i,k+1/2}), \tag{38}$$

$$\eta^{\psi\psi}_{i+1/2,k}(m) \equiv \frac{1}{\Delta z}\left\langle \phi_k(z)\varepsilon(i\Delta x,z)\middle|\tilde{\psi}_{k-m}(z)\right\rangle = h^*_{-2m+1}(\varepsilon_{i+1/2,k-m+1/2} - \varepsilon_{i+1/2,k}). \tag{39}$$

An important observation here is that (25) represents the 'local' relation of only $\phi(x)\phi(z)$ terms and it does not involve other wavelet terms, while (33) and (34) involve $E^{y,\phi\phi}$, and (35) involves $E^{y,\phi\phi}$, $E^{y,\phi\psi}$ and $E^{y,\psi\phi}$. If other types of wavelets are used as the basis and the weighted inner products as in (23) and (29) do not vanish, then (25) and (33)–(35) result in a system of equations to be solved or in a quadrature formula to be computed at every time step. For multi-dimensional problems, this often results in a significant computational overhead and the efficiency of the method will be reduced. In contrast, the proposed method has reduced this overhead and the associated complicated numerical implimentation.

Next we discretize Ampere's law (13). Testing each side of (13) with $\tilde{\phi}_{i'}\tilde{\phi}_{k'}h_{n'}$ leads to

$$\left\langle J_y\middle|\tilde{\phi}_{i'}\tilde{\phi}_{k'}h_{n'}\right\rangle + \frac{\sigma}{\varepsilon}\left\langle D_y\middle|\tilde{\phi}_{i'}\tilde{\phi}_{k'}h_{n'}\right\rangle + \left\langle \frac{\partial D_y}{\partial t}\middle|\tilde{\phi}_{i'}\tilde{\phi}_{k'}h_{n'}\right\rangle = \left\langle \frac{\partial H_x}{\partial z}\middle|\tilde{\phi}_{i'}\tilde{\phi}_{k'}h_{n'}\right\rangle - \left\langle \frac{\partial H_z}{\partial x}\middle|\tilde{\phi}_{i'}\tilde{\phi}_{k'}h_{n'}\right\rangle. \tag{40}$$

Substituting the field expansions (17), (19) and (20) to (40), and considering the biorthogonality relation (8), we obtain

$$\begin{aligned}
&\sum_{i,k,n=-\infty}^{+\infty}\left[\left(J^{y,\phi\phi}_{i,k,n+1/2} + \frac{\sigma}{\varepsilon}D^{y,\phi\phi}_{i,k,n+1/2}\right)\langle h_{n+1/2}|h_{n'}\rangle + D^{y,\phi\phi}_{i,k,n+1/2}\left\langle \frac{\mathrm{d}h_{n+1/2}}{\mathrm{d}t}\middle|h_{n'}\right\rangle\right]\Delta x\Delta z\delta_{ii'}\delta_{kk'} \\
&= \sum_{i,k,n=-\infty}^{+\infty}\left[H^{x,\phi\phi}_{i,k+1/2,n}\left\langle \frac{\mathrm{d}\phi_{k+1/2}}{\mathrm{d}z}\middle|\tilde{\phi}_{k'}\right\rangle + H^{x,\phi\psi}_{i,k+1,n}\left\langle \frac{\mathrm{d}\psi_{k+1/2}}{\mathrm{d}z}\middle|\tilde{\phi}_{k'}\right\rangle\right]\Delta x\Delta t\delta_{ii'}\delta_{nn'} \\
&\quad - \sum_{i,k,n=-\infty}^{+\infty}\left[H^{z,\phi\phi}_{i+1/2,k,n}\left\langle \frac{\mathrm{d}\phi_{i+1/2}}{\mathrm{d}x}\middle|\tilde{\phi}_{i'}\right\rangle + H^{z,\psi\phi}_{i+1,k,n}\left\langle \frac{\mathrm{d}\psi_{i+1/2}}{\mathrm{d}x}\middle|\tilde{\phi}_{i'}\right\rangle\right]\Delta z\Delta t\delta_{kk'}\delta_{nn'}.
\end{aligned} \tag{41}$$

To calculate the inner products in (41), we define connection coefficients between the derivative of the basis functions and the dual basis functions as

$$a_{\phi\phi}(l) \equiv \left\langle \frac{\mathrm{d}\phi_{i+1/2}}{\mathrm{d}x} \middle| \tilde{\phi}_{i-l} \right\rangle = \left. \frac{\mathrm{d}\phi(x)}{\mathrm{d}x} \right|_{x=-l-(1/2)}, \tag{42}$$

$$a_{\phi\psi}(l) \equiv \left\langle \frac{\mathrm{d}\phi_{i+1/2}}{\mathrm{d}x} \middle| \tilde{\psi}_{i-l} \right\rangle = \sum_{k=-2p+2}^{2p} (-1)^{k-1} h^*_{-k+1} \left. \frac{\mathrm{d}\phi(x)}{\mathrm{d}x} \right|_{x=-l+(k/2)-(1/2)}, \tag{43}$$

$$a_{\psi\phi}(l) \equiv \left\langle \frac{\mathrm{d}\psi_{i+1/2}}{\mathrm{d}x} \middle| \tilde{\phi}_{i-l} \right\rangle = 2 \left. \frac{\mathrm{d}\phi(x)}{\mathrm{d}x} \right|_{x=-2l-2}, \tag{44}$$

$$a_{\psi\psi}(l) \equiv \left\langle \frac{\mathrm{d}\psi_{i+1/2}}{\mathrm{d}x} \middle| \tilde{\psi}_{i-l} \right\rangle = 2 \sum_{k=-2p+2}^{2p} (-1)^{k-1} h^*_{-k+1} \left. \frac{\mathrm{d}\phi(x)}{\mathrm{d}x} \right|_{x=-2l+k-2}. \tag{45}$$

In the above inner products we assumed Δx to be unity. They have been eveluated numerically and are listed for $p = 2, 4$ and 10 in Tables 2–4. The inner products in (41) are then given by

$$\left\langle \frac{\mathrm{d}\phi_{i+1/2}}{\mathrm{d}x} \middle| \tilde{\phi}_{i'} \right\rangle = \sum_l a_{\phi\phi}(l) \delta_{i,i'+l}, \tag{46}$$

$$\left\langle \frac{\mathrm{d}\phi_{i+1/2}}{\mathrm{d}x} \middle| \tilde{\psi}_{i'} \right\rangle = \sum_l a_{\phi\psi}(l) \delta_{i,i'+l}, \tag{47}$$

$$\left\langle \frac{\mathrm{d}\psi_{i+1/2}}{\mathrm{d}x} \middle| \tilde{\phi}_{i'} \right\rangle = \sum_l a_{\psi\phi}(l) \delta_{i,i'+l}, \tag{48}$$

$$\left\langle \frac{\mathrm{d}\psi_{i+1/2}}{\mathrm{d}x} \middle| \tilde{\psi}_{i'} \right\rangle = \sum_l a_{\psi\psi}(l) \delta_{i,i'+l}. \tag{49}$$

Table 2
Connection coefficients for the interpolating basis DD_2

$p = 2$				
l	$a_{\phi\phi}$	$a_{\phi\psi}$	$a_{\psi\phi}$	$a_{\psi\psi}$
−4		−0.0006510		
−3	−0.0104167	0.0117187		0.0104167
−2	0.0937500	−0.0403643	0.1666666	−0.0937500
−1	−1.2291667	0.0481768	0.0	−1.4374998
0	1.2291667	0.0	−0.1666666	1.4374998
1	−0.0937500	−0.0481768		0.0937500
2	0.0104167	0.0403643		−0.0104167
3		−0.0117187		
4		0.0006510		

Table 3
Connection coefficients for the interpolating basis DD_4

$p = 4$				
l	$a_{\phi\phi}$	$a_{\phi\psi}$	$a_{\psi\phi}$	$a_{\psi\psi}$
−8		−0.0000018		
−7		0.0000397		
−6	−0.0000109	−0.0004033		0.0000109
−5	−0.0008309	0.0030967		0.0008309
−4	0.0086543	−0.0144141	−0.0000017	−0.0086543
−3	−0.0419957	0.0394952	0.0044481	0.0426846
−2	0.1560101	−0.0637289	0.3839979	−0.2903309
−1	−1.3110341	0.0533016	0.0	−1.8610039
0	1.3110341	0.0	−0.3839979	1.8610039
1	−0.1560101	−0.0533016	−0.0044481	0.2903309
2	0.0419957	0.0637289	0.0000017	−0.0426846
3	−0.0086543	−0.0394952		0.0086543
4	0.0008309	0.0144141		−0.0008309
5	0.0000109	−0.0030967		−0.0000109
6		0.0004033		
7		−0.0000397		
8		0.0000018		

For the rectangular pulse function $h_n(t)$, it can be shown that

$$\left\langle \frac{\mathrm{d}h_{n+1/2}}{\mathrm{d}t} \middle| h_{n'} \right\rangle = \delta_{nn'} - \delta_{n,n'-1}, \tag{50}$$

$$\left\langle h_{n+1/2} \middle| h_{n'} \right\rangle = \frac{1}{2}\left(\delta_{nn'} + \delta_{n,n'-1}\right)\Delta t. \tag{51}$$

Substituting (46)–(51) to (41) leads to

$$\begin{aligned}
&\sum_{i,k,n=-\infty}^{+\infty}\left[\left(J^{y,\phi\phi}_{i,k,n+1/2} + \frac{\sigma}{\varepsilon}D^{y,\phi\phi}_{i,k,n+1/2}\right)\frac{1}{2}\Delta t\left(\delta_{nn'} + \delta_{n,n'-1}\right) + D^{y,\phi\phi}_{i,k,n+1/2}\left(\delta_{nn'} - \delta_{n,n'-1}\right)\right]\Delta x\Delta z\delta_{ii'}\delta_{kk'} \\
&\quad = \sum_{i,k,n=-\infty}^{+\infty}\left[H^{x,\phi\phi}_{i,k+1/2,n}\sum_l a_{\phi\phi}(l)\delta_{k,k'+l} + H^{x,\phi\psi}_{i,k+1,n}\sum_l a_{\psi\phi}(l)\delta_{k,k'+l}\right]\Delta x\Delta t\delta_{ii'}\delta_{nn'} \\
&\qquad - \sum_{i,k,n=-\infty}^{+\infty}\left[H^{z,\phi\phi}_{i+1/2,k,n}\sum_l a_{\phi\phi}(l)\delta_{i,i'+l} + H^{z,\psi\phi}_{i+1,k,n}\sum_l a_{\psi\phi}(l)\delta_{i,i'+l}\right]\Delta z\Delta t\delta_{kk'}\delta_{nn'}
\end{aligned} \tag{52}$$

or

$$\begin{aligned}
&\left[J^{y,\phi\phi}_{i,k,n}\Delta t + \frac{\sigma}{2\varepsilon}\left(D^{y,\phi\phi}_{i,k,n+1/2} + D^{y,\phi\phi}_{i,k,n-1/2}\right)\Delta t + D^{y,\phi\phi}_{i,k,n+1/2} - D^{y,\phi\phi}_{i,k,n-1/2}\right]\Delta x\Delta z \\
&\quad = \left[\sum_l a_{\phi\phi}(l)H^{x,\phi\phi}_{i,k+1/2+l,n} + \sum_l a_{\psi\phi}(l)H^{x,\phi\psi}_{i,k+1+l,n}\right]\Delta x\Delta t \\
&\qquad - \left[\sum_l a_{\phi\phi}(l)H^{z,\phi\phi}_{i+1/2+l,k,n} + \sum_l a_{\psi\phi}(l)H^{z,\psi\phi}_{i+1+l,k,n}\right]\Delta z\Delta t.
\end{aligned} \tag{53}$$

The rest of the wavelet coefficients can be obtained similarly.

Table 4
Connection coefficients for the interpolating basis DD_{10}

$p = 10$				
l	$a_{\phi\phi}$	$a_{\phi\psi}$	$a_{\psi\phi}$	$a_{\psi\psi}$
−14		−0.0000002		
−13		−0.0000013		
−12		−0.0000067		
−11	−0.0000003	0.0000288		0.0000003
−10	0.0000008	−0.0001107		−0.0000008
−9	−0.0000179	0.0003871		0.0000179
−8	0.0001584	−0.0012294		−0.0001584
−7	−0.0008675	0.0034617		0.0008675
−6	0.0034152	−0.0083777	0.0000005	−0.0034153
−5	−0.0104550	0.0169735	0.0001534	0.0104330
−4	0.0265750	−0.0281547	0.0070521	−0.0290999
−3	−0.0616128	0.0372116	0.0968546	0.0029354
−2	0.1636942	−0.0371457	0.6695688	−0.6999128
−1	−1.3033236	0.0236495	0.0	−2.3169613
0	1.3033236	0.0	−0.6695688	2.3169613
1	−0.1636942	−0.0236495	−0.0968546	0.6999128
2	0.0616128	0.0371457	−0.0070521	−0.0029354
3	−0.0265750	−0.0372116	−0.0001534	0.0290999
4	0.0104550	0.0281547	−0.0000005	−0.0104330
5	−0.0034152	−0.0169735		0.0034153
6	0.0008675	0.0083777		−0.0008675
7	−0.0001584	−0.0034617		0.0001584
8	0.0000179	0.0012294		−0.0000179
9	−0.0000008	−0.0003871		0.0000008
10	0.0000003	0.0001107		−0.0000003
11		−0.0000288		
12		0.0000067		
13		0.0000013		
14		0.0000002		

Coefficients smaller than 10^{-7} have been truncated.

Substituting (25) and (33)–(35) into (52) and its counterparts for other wavelet coefficients, we eliminate the flux density D_y from the final time evolution equations as

$$E^{y,\phi\phi}_{i,k,n+1/2} = \frac{2\varepsilon - \sigma\Delta t}{2\varepsilon + \sigma\Delta t} E^{y,\phi\phi}_{i,k,n-1/2} + \frac{2\Delta t}{2\varepsilon + \sigma\Delta t}\left\{ \frac{1}{\Delta z}\left[\sum_l a_{\phi\phi}(l) H^{x,\phi\phi}_{i,k+l+1/2,n} + \sum_l a_{\psi\phi}(l) H^{x,\phi\psi}_{i,k+l+1,n} \right] - \frac{1}{\Delta x}\left[\sum_l a_{\phi\phi}(l) H^{z,\phi\phi}_{i+l+1/2,k,n} + \sum_l a_{\psi\phi}(l) H^{z,\psi\phi}_{i+l+1,k,n} \right] - J^{y,\phi\phi}_{i,k,n} \right\}, \tag{54}$$

$$E^{y,\phi\psi}_{i,k+1/2,n+1/2} = \frac{2\varepsilon - \sigma\Delta t}{2\varepsilon + \sigma\Delta t}\left(E^{y,\phi\psi}_{i,k+1/2,n-1/2} + \Upsilon^{y,\phi\psi}_{i,k+1/2,n-1/2} \right) - \Upsilon^{y,\phi\psi}_{i,k+1/2,n+1/2} + \frac{2\Delta t}{2\varepsilon + \sigma\Delta t}\left\{ \frac{1}{\Delta z}\left[\sum_l a_{\phi\psi}(l) H^{x,\phi\phi}_{i,k+l+1/2,n} + \sum_l a_{\psi\psi}(l) H^{x,\phi\psi}_{i,k+l+1,n} \right] - \frac{1}{\Delta x}\left[\sum_l a_{\phi\phi}(l) H^{z,\phi\psi}_{i+l+1/2,k+1/2,n} + \sum_l a_{\psi\phi}(l) H^{z,\psi\psi}_{i+l+1,k+1/2,n} \right] - J^{y,\phi\psi}_{i,k+1/2,n} \right\}, \tag{55}$$

$$E^{y,\psi\phi}_{i+1/2,k,n+1/2} = \frac{2\varepsilon-\sigma\Delta t}{2\varepsilon+\sigma\Delta t}\left(E^{y,\psi\phi}_{i+1/2,k,n-1/2}+\Upsilon^{y,\psi\phi}_{i+1/2,k,n-1/2}\right)-\Upsilon^{y,\psi\phi}_{i+1/2,k,n+1/2} + \frac{2\Delta t}{2\varepsilon+\sigma\Delta t}\left\{\frac{1}{\Delta z}\left[\sum_l a_{\phi\phi}(l)H^{x,\psi\phi}_{i+1/2,k+l+1/2,n}+\sum_l a_{\psi\phi}(l)H^{x,\psi\psi}_{i+1/2,k+l+1,n}\right] - \frac{1}{\Delta x}\left[\sum_l a_{\phi\psi}(l)H^{z,\phi\phi}_{i+l+1/2,k,n}+\sum_l a_{\psi\psi}(l)H^{z,\psi\phi}_{i+l+1,k,n}\right]-J^{y,\psi\phi}_{i+1/2,k,n}\right\}, \tag{56}$$

$$E^{y,\psi\psi}_{i+1/2,k+1/2,n+1/2} = \frac{2\varepsilon-\sigma\Delta t}{2\varepsilon+\sigma\Delta t}\left(E^{y,\psi\psi}_{i+1/2,k+1/2,n-1/2}+\Upsilon^{y,\psi\psi}_{i+1/2,k+1/2,n-1/2}\right)-\Upsilon^{y,\psi\psi}_{i+1/2,k+1/2,n+1/2} + \frac{2\Delta t}{2\varepsilon+\sigma\Delta t}\left\{\frac{1}{\Delta z}\left[\sum_l a_{\phi\psi}(l)H^{x,\psi\phi}_{i+1/2,k+l+1/2,n}+\sum_l a_{\psi\psi}(l)H^{x,\psi\psi}_{i+1/2,k+l+1,n}\right] - \frac{1}{\Delta x}\left[\sum_l a_{\phi\psi}(l)H^{z,\phi\psi}_{i+l+1/2,k+1/2,n}+\sum_l a_{\psi\psi}(l)H^{z,\psi\psi}_{i+l+1,k+1/2,n}\right]-J^{y,\psi\psi}_{i+1/2,k+1/2,n}\right\}, \tag{57}$$

where

$$\Upsilon^{y,\phi\psi}_{i,k+1/2,n+1/2} = \sum_{l=-p+1}^{p}\frac{\eta^{\phi\psi}_{i,k}(l)}{\varepsilon_{i,k+1/2}}E^{y,\phi\phi}_{i,k+l,n+1/2}, \tag{58}$$

$$\Upsilon^{y,\psi\phi}_{i+1/2,k,n+1/2} = \sum_{l=-p+1}^{p}\frac{\eta^{\psi\phi}_{i,k}(l)}{\varepsilon_{i+1/2,k}}E^{y,\phi\phi}_{i+l,k,n+1/2}, \tag{59}$$

$$\Upsilon^{y,\psi\psi}_{i+1/2,k+1/2,n+1/2} = \sum_{l=-p+1}^{p}\sum_{m=-p+1}^{p}\frac{\eta^{\psi\psi}_{i,k}(l,m)}{\varepsilon_{i+1/2,k+1/2}}E^{y,\phi\phi}_{i+l,k+m,n+1/2}+\sum_{l=-p+1}^{p}\frac{\eta^{\psi\psi}_{i,k+1/2}(l)}{\varepsilon_{i+1/2,k+1/2}}E^{y,\phi\psi}_{i+l,k+1/2,n+1/2} + \sum_{m=-p+1}^{p}\frac{\eta^{\psi\psi}_{i+1/2,k}(m)}{\varepsilon_{i+1/2,k+1/2}}E^{y,\psi\phi}_{i+1/2,k+m,n+1/2} \tag{60}$$

are the inhomogeneity correction terms that are non-zeros in the vicinity of dielectric interface over $2p-1$ cells and vanish in a homogeneous dielectric region; the summation is taken for $l=[-p+1,p]$ with p being the index of the scaling function. The other field components of $E^{y,\psi\phi}$, $E^{y,\psi\psi}$, and those for H_x and H_z can be obtained similarly. For reader's convenience the discrete forms of Faraday's law (11) and (12) are given in the followings, which completes together with (54)–(60) the time-evolution equations of the proposed method:

$$H^{x,\phi\phi}_{i,k+1/2,n+1} = H^{x,\phi\phi}_{i,k+1/2,n}+\frac{\Delta t}{\mu\Delta z}\left[\sum_l a_{\phi\phi}(l)E^{y,\phi\phi}_{i,k+l+1,n+1/2}+\sum_l a_{\psi\phi}(l)E^{y,\phi\psi}_{i,k+l+3/2,n+1/2}\right], \tag{61}$$

$$H^{x,\phi\psi}_{i,k+1,n+1} = H^{x,\phi\psi}_{i,k+1,n}+\frac{\Delta t}{\mu\Delta z}\left[\sum_l a_{\phi\psi}(l)E^{y,\phi\phi}_{i,k+l+1,n+1/2}+\sum_l a_{\psi\psi}(l)E^{y,\phi\psi}_{i,k+l+3/2,n+1/2}\right], \tag{62}$$

$$H^{x,\psi\phi}_{i+1/2,k+1/2,n+1} = H^{x,\psi\phi}_{i+1/2,k+1/2,n}+\frac{\Delta t}{\mu\Delta z}\left[\sum_l a_{\phi\phi}(l)E^{y,\psi\phi}_{i+1/2,k+l+1,n+1/2}+\sum_l a_{\psi\phi}(l)E^{y,\psi\psi}_{i+1/2,k+l+3/2,n+1/2}\right], \tag{63}$$

$$H^{x,\psi\psi}_{i+1/2,k+1,n+1} = H^{x,\psi\psi}_{i+1/2,k+1,n} \frac{\Delta t}{\mu \Delta z} \left[\sum_l a_{\phi\psi}(l) E^{y,\psi\phi}_{i+1/2,k+l+1,n+1/2} + \sum_l a_{\psi\psi}(l) E^{y,\psi\psi}_{i+1/2,k+l+3/2,n+1/2} \right], \tag{64}$$

$$H^{z,\phi\phi}_{i+1/2,k,n+1} = H^{z,\phi\phi}_{i+1/2,k,n} - \frac{\Delta t}{\mu \Delta x} \left[\sum_l a_{\phi\phi}(l) E^{y,\phi\phi}_{i+l+1,k,n+1/2} + \sum_l a_{\psi\phi}(l) E^{y,\psi\phi}_{i+l+3/2,k,n+1/2} \right], \tag{65}$$

$$H^{z,\phi\psi}_{i+1/2,k+1/2,n+1} = H^{z,\phi\psi}_{i+1/2,k+1/2,n} - \frac{\Delta t}{\mu \Delta x} \left[\sum_l a_{\phi\phi}(l) E^{y,\phi\psi}_{i+l+1,k+1/2,n+1/2} + \sum_l a_{\psi\phi}(l) E^{y,\psi\psi}_{i+l+3/2,k+1/2,n+1/2} \right], \tag{66}$$

$$H^{z,\psi\phi}_{i+1,k,n+1} = H^{z,\psi\phi}_{i+1,k,n} - \frac{\Delta t}{\mu \Delta x} \left[\sum_l a_{\phi\psi}(l) E^{y,\phi\phi}_{i+l+1,k,n+1/2} + \sum_l a_{\psi\psi}(l) E^{y,\psi\phi}_{i+l+3/2,k,n+1/2} \right], \tag{67}$$

$$H^{z,\psi\psi}_{i+1,k+1/2,n+1} = H^{z,\psi\psi}_{i+1,k+1/2,n} - \frac{\Delta t}{\mu \Delta x} \left[\sum_l a_{\phi\psi}(l) E^{y,\phi\psi}_{i+l+1,k+1/2,n+1/2} + \sum_l a_{\psi\psi}(l) E^{y,\psi\psi}_{i+l+3/2,k+1/2,n+1/2} \right], \tag{68}$$

where μ is the magnetic permeability of the media, which is assumed to be homogeneous over the analysis region.

Note that the formulation presented here is versatile in terms of the inhomogeneity of the media; the scaling function coefficients $E^{y,\phi\phi}$ are first updated throughout the analysis region, then the wavelet coefficients $E^{y,\phi\psi}$ and $E^{y,\psi\phi}$ can be updated using the scaling function coefficients already updated. and finally $E^{y,\psi\psi}$ is updated using $E^{y,\phi\phi}$, $E^{y,\phi\psi}$ and $E^{y,\psi\phi}$, which have been just updated. Although additional memory is required to store the inhomogeneity correction terms Υ for the previous time step instead of D_y, the wavelet terms can be applied locally within the limited sub-regions expected according to the a priori knowledge of the field distribution, resulting in an effective sub-gridding algorithm.

Again, this procedure serves to reduce the overhead of solving a system of equations to obtain the coefficients of E^y from those of D^y even for inhomogeneous dielectric regions. The summations with respect to the stencil l in (54) to (68) are taken according to the number of the connection coefficients $a_{\xi\zeta}(l)$ for $\xi, \zeta = \phi, \psi$.

2.3. Numerical dispersion analysis and stability criteria

For simplicity we assume square cells $\Delta x = \Delta z \equiv \Delta$ are used, then the numerical dispersion relation of the proposed method based on the scaling functions is obtained by substituting a time-harmonic trial solution to the time evolution difference Eqs. (54), (61) and (65), yielding

$$\left(\frac{\Delta}{c\Delta t}\right)^2 \sin^2\left(\frac{\Omega}{2}\right) = \left\{ \sum_{l=0}^{L-1} a_{\phi\phi}(l) \sin\left[\chi(\sin\theta)\left(l+\frac{1}{2}\right)\right] \right\}^2 + \left\{ \sum_{l=0}^{L-1} a_{\phi\phi}(l) \sin\left[\chi(\cos\theta)\left(l+\frac{1}{2}\right)\right] \right\}^2, \tag{69}$$

where c is the speed of light, θ the angle of propagation, L the stencil size of $a_{\phi\phi}$, and Ω and χ being the normalized angular frequency and the wavenumber, respectively, related to the real angular frequency ω and the wave vector $\boldsymbol{k}$ by

$$\Omega = \omega \Delta t \tag{70}$$

and

$$\chi = |\boldsymbol{k}|\Delta. \tag{71}$$

It is implied in (69) that the dispersion relation between Ω and χ is dependent on the set of the connection coefficients $a_{\phi\phi}(l)$, the angle θ and the ratio between Δt and Δ, which is referred to as the stability factor

$$s \equiv \frac{c\Delta t}{\Delta}. \tag{72}$$

To maintain stable computation, the time step Δt has a maximum allowable value determined by the stability factor s. The stability criteria has been derived for the Battle–Lemarié wavelets in [5,17]. The stability criteria for the present method is also obtained by requiring that (68) has a solution for real frequencies for all wave numbers. For the present method based on the scaling functions, we obtain

$$\Delta t \leqslant \left[c \left(\sum_{l=0}^{L} |a_{\phi\phi}(l)| \right) \sqrt{\left(\frac{1}{\Delta x}\right)^2 + \left(\frac{1}{\Delta z}\right)^2} \right]^{-1}. \tag{73}$$

For $\Delta x = \Delta z \equiv \Delta$ (73) reduces to

$$\Delta t \leqslant s_{\phi\phi} \frac{\Delta}{c} \tag{74}$$

with

$$s_{\phi\phi} = \left(\sqrt{2} \sum_{l=0}^{L-1} |a_{\phi\phi}(l)| \right)^{-1}. \tag{75}$$

For the scheme containing the wavelet functions both in the x- and z-directions, the stability criterion has been obtained again in [5,17] as

$$s_{\psi\psi} = \sqrt{2} \left[\left(\sum_l |a_{\phi\phi}(l)| \right)^2 + 2 \sum_l |a_{\phi\psi}(l)| \cdot \sum_l |a_{\psi\phi}(l)| + \left(\sum_l |a_{\psi\psi}(l)| \right)^2 + \left(\sum_l |a_{\phi\phi}(l) + a_{\psi\psi}(l)| \right) \cdot \sqrt{\left(\sum_l |a_{\phi\phi}(l) - a_{\psi\psi}(l)| \right)^2 + 4 \sum_l |a_{\phi\psi}(l)| \cdot \sum_l |a_{\psi\phi}(l)|} \right]^{-1/2}. \tag{76}$$

Table 5 lists the stability factors obtained with (74) and (76). The stability factor for the three-dimensional case is obtained by multiplying (74) or (76) by factor $\sqrt{2/3}$.

To depict the numerical dispersion of the proposed scheme based on the scaling function, the nonlinear Eq. (69) is solved numerically. The frequency errors from the linear dispersion $\omega^2/c^2 = k_x^2 + k_z^2$ are then plotted in Fig. 3(a) for the axial propagation where a plane wave propagates along the main grid axis, and in Fig. 3(b) for the diagonal propagation where a plane wave propagates at 45° with respect to the grid axis. For both cases $s = 0.1$ is used; preliminary experiments have shown that it is not advantageous to take the maximum allowable stability factor due to the deterioration of the accuracy.

Note that the standard finite-difference method has the exact linear dispersion for the diagonal propagation when s is the maximum allowable value ($1/\sqrt{2}$), while highly dispersive for the axial propagation. The higher-order schemes have similar errors for both the diagonal and the axial propagation. The pro-

Table 5
Maximum allowable stability factor for the DD_p scheme with $p = 2$, 4 and 10

p	2D		3D	
	$s_{\phi\phi}$	$s_{\psi\psi}$	$s_{\phi\phi}$	$s_{\psi\psi}$
2	0.530	0.426	0.433	0.348
4	0.466	0.295	0.380	0.241
10	0.450	0.213	0.368	0.174

The two-dimensional (2D) and the three-dimensional (3D) cases are shown.

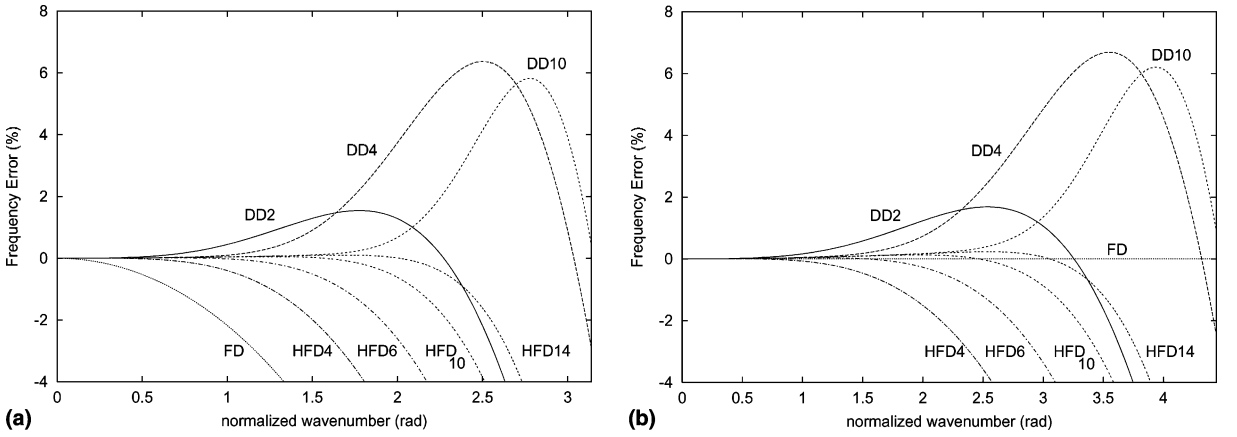

Fig. 3. Numerical dispersion relation of the proposed method based on the scaling function. The stability factor is $s = 0.1$ except for the standard finite-difference (FD) scheme where $s = 1/\sqrt{2}$. (a) is for the axial propagation, and (b) for the diagonal propagation.

posed scheme based on the DD_2, DD_4 and DD_{10} scaling functions have the accuracy approximately comparable to the fourth, sixth and tenth higher-order finite-difference schemes, respectively.

We then evaluate the numerical errors by analyzing the resonant frequency of a resonant frequency of a square cavity. We have analyzed a resonant frequency of a square cavity by changing the resolution and the basis functions involved. The size of the cavity was $1/\sqrt{2} \times 1/\sqrt{2}$ and the normalized dominant resonant frequency was unity. Because the dominant TE_{11} mode is considered to be a superposition of plane waves propagating at 45° with respect to the grid axis, it corresponds to the dispersion error of the diagonal propagation. Figs. 4(a) and (b) show the resulting frequency errors of the dominant resonant mode as a function of the number of cells per dimension N obtained with the scaling function only, and with both the scaling and the wavelet functions, respectively. For non-integer values $N = 1.5$ and 1.25, square cavitys of size $2m/\sqrt{2} \times 2m/\sqrt{2}$ with $m = 1, 2$ were analyzed with $(2m + 1) \times (2m + 1)$ cells for the higher-order $TE_{2m,2m}$ mode. The stability factor was chosen to be $s = 0.1$. The resonant frequency was extracted by detecting the maximum peak in the Fourier spectrum of the time signal which has been measured for a sufficiently long time for the peak location to converge.

As shown in Fig. 4(a), higher-order function gives higher accuracy, while DD_2 has small errors for $N = 1.5$ and 1.25; these results agree to those of the dispersion analysis in Fig. 3(a). Since the wave number for the diagonal propagation is $k = \sqrt{(k_x)^2 + (k_z)^2} = \sqrt{2}\pi/(N\Delta)$, the normalized wave number χ is related to the number of cells N by $\chi = k\Delta = \sqrt{2}\pi/N$. Fig. 4(b) shows that when the wavelets are added, the DD_4 and DD_{10} have similar accuracy and that they both have small errors even for the small N such as $N = 1.5$ and 1.25, while DD_2 still has relatively large errors.

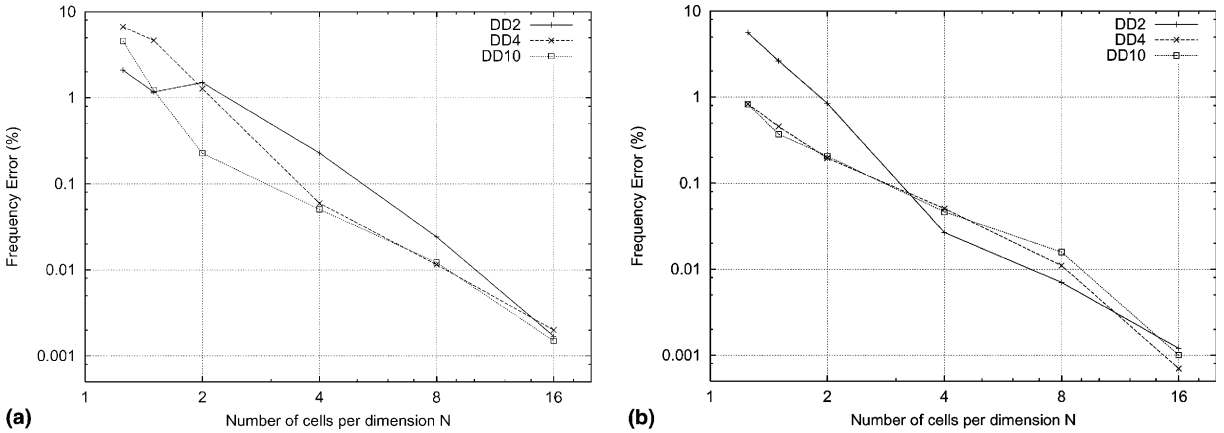

Fig. 4. Frequency errors in the analysis of a square cavity resonator. (a) Only the scaling function $\phi(x)\phi(z)$ is used. (b) Both the scaling function $\phi(x)\phi(z)$ and the wavelets $\phi(x)\psi(z)$, $\psi(x)\phi(z)$ are used. The reference resonant frequency is unity. The stability factor is $s = 0.1$.

3. Numerical experiments

3.1. Analysis of dielectric waveguides

A dielectric waveguide with a core region of corrugated dielectric constants depicted in Fig. 5 has been tested with the proposed scheme using DD_4 and the conventional FDTD method [9]. The waveguide is surrounded by ten layers of the anisotropic perfectly matched layer (APML) absorbing boundary conditions (ABCs) [22]. The APML ABC in the present scheme has been implemented for the scaling coefficients only and the typical reflection from the boundary is in the range of −50 dB for five layers and −80 dB for 10 layers [14,15]. The ABC region is backed by the perfect electric conductors that are implemented by means of the mirror principle, namely imposing odd symmetry for the tangential electric field and even symmetry for the tangential magnetic field.

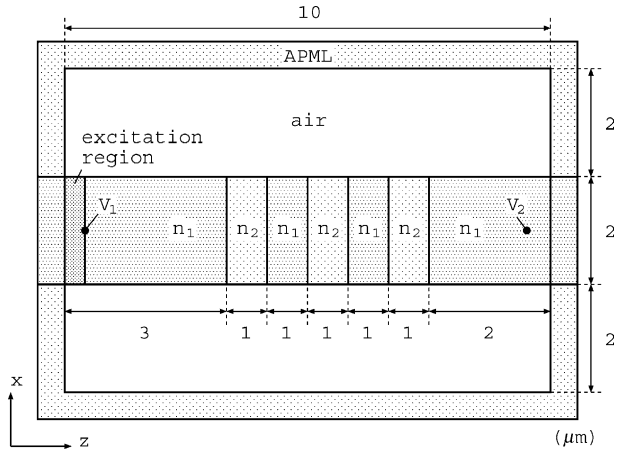

Fig. 5. Dielectric waveguide tested. Refractive indexes are $n_1 = 3$ and $n_2 = 2.828$.

Table 6
Analysis conditions for the dielectric waveguide of Fig. 5

	Scheme	Δx (μm)	Δz (μm)	Time steps (s)	CPU time (s)	Memory (MBytes)
(i)	FDTD	0.025	0.0125	4022	305	49
(ii)	FDTD	0.05	0.025	2011	55	25
(iii)	DD_4, $\phi\phi$ only	0.1	0.05	5028	57	14
(iv)	DD_4, $\phi\phi$ only	0.1	0.1	3180	22	8.4
(v)	DD_4, $\phi\phi$ and $\phi\psi$	0.1	0.1	3180	32	8.4
(vi)	DD_4, $\phi\phi$, $\phi\psi$ and $\psi\phi$	0.2	0.1	2514	21	8.4

Several analysis conditions with different resolution levels were tested as in Table 6. Cases (i) and (ii) are for the standard FDTD method, and (iii) and (iv) are for the present method based on the DD_4 scaling function. In (v), the wavelet term $\phi(x)\psi(z)$ was added for the core region of the waveguide where the major part of the energy propagates and finer resolution is desired; this is equivalent to the sub-gridding technique of the conventional finite-difference methods. The $\phi(x)\psi(z)$ coefficients are 33% of the underlying scaling function coefficients in number. In (vi), additional wavelet term $\psi(x)\phi(z)$ was employed for the region 1.2 times wider than the core region, i.e., for the 2.4 μm-wide center region. The $\psi(x)\phi(z)$ wavelet coefficients are 40% of the scaling function coefficients in number. For the FDTD (i) and (ii), the discretization must be significantly finer than the present method, resulting in excessive computational expenditure for practical problems.

Time function $f(t) = -\sin(\omega_0 t)\sin^2(0.1\omega_0 t)$ with the center frequency $\omega_0 = 2\pi f_0, f_0 = 193$ THz fo $0 < t < 5T$, $T = 1/f_0 = 5.18$ fs was applied to launch the pulse at the excitation region of the waveguide. For the results shown in Fig. 8, good convergence has been obtained except (iv) with the proposed scheme based on DD_4, while not yet obtained with the conventional FDTD method even with much finer resolution as shown in Fig. 7. For the resolution (iv), where the grid is relatively coarse and only the scaling function is employed, the resulting time data in Fig. 8 has been too oscillatory due to the numerical dispersion error. However, the addition of the wavelet coefficients $\psi(x)\phi(z)$ in (v) has improved the result compared to that of (iv). When the grid is coarsened in the x-direction in (vi), the time signals are slightly distorted in the tail; this can be due to the reflection from the waveguide side walls; note that the main pulse still remains convergent in those cases. Good agreement is demonstrated in Fig. 9 for the results of the present scheme and the conventional FDTD when they converge with the sufficiently fine resolution.

The E_y field coefficients are plotted in Figs. 6(a) and (b). It is found in Fig. 6(b) that $E_y^{\phi\psi}$ is less than 1% of $E_y^{\phi\phi}$ in magnitude even in the core waveguide region, and that it is reasonable and efficient to ignore $E_y^{\phi\psi}$ in the clad (air) region in this case.

The computation was performed on an IBM super computer 'Minerva' at the University of Victoria, BC, Canada, which has a massively parallel architecture with 16 processors operated at 375 MHz clock rate, but only a single processor is used for this evaluation purpose. The computational requirements listed in Table 6 are based on a program code that has not yet been fully optimized; however, the results still give good estimates for the practical implementation. The computational resources are significantly reduced in the present method because it employs a much coarser grid than in the standard FDTD method while maintaining their accuracy; moreover, a coarser grid allows larger time step, thus reducing the number of time steps to simulate a certain time period. The number of unknowns are reduced by one to two orders of magnitude; the present scheme of (v) requires only about one ninth of CPU time and one fifth of memory of those of FDTD (i). Note that the memory requirement is dependent on the resolution, not on the basis functions used; if the resolution is the same, then the memory requirement is also the same even for the different basis functions are used.

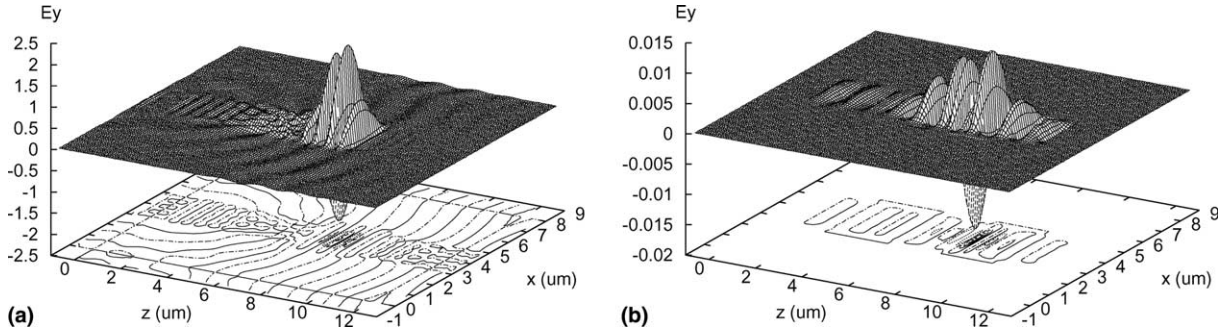

Fig. 6. Distribution of: (a) the scaling function coefficient $E^{y,\phi\phi}$ and (b) the wavelet coefficient $E^{y,\phi\psi}$ obtained with DD_4 (v) with 0.1×0.1 μm^2 grid.

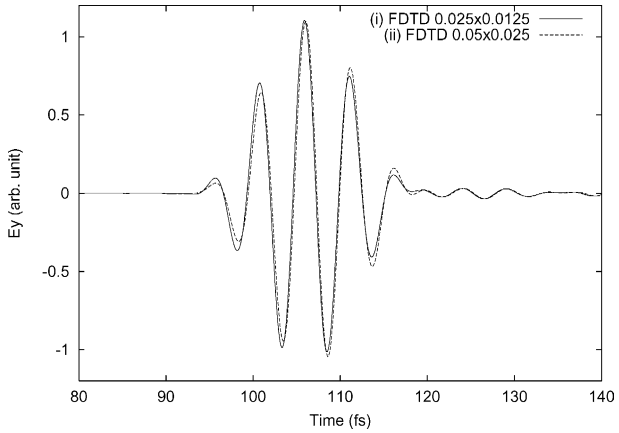

Fig. 7. Time series data of the dielectric waveguide obtained with FDTD at point V_2.

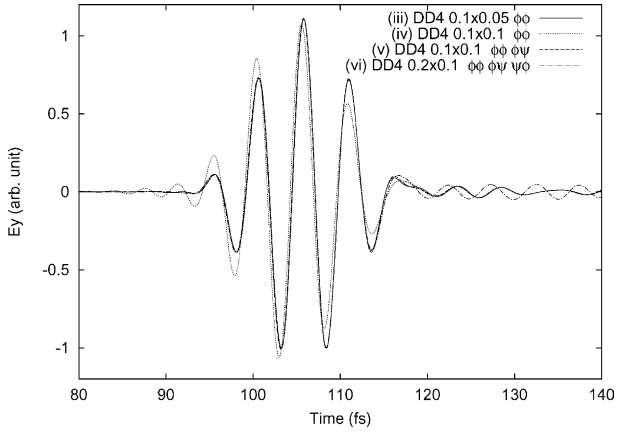

Fig. 8. Time series data of the dielectric waveguide obtained with DD_4 at point V_2.

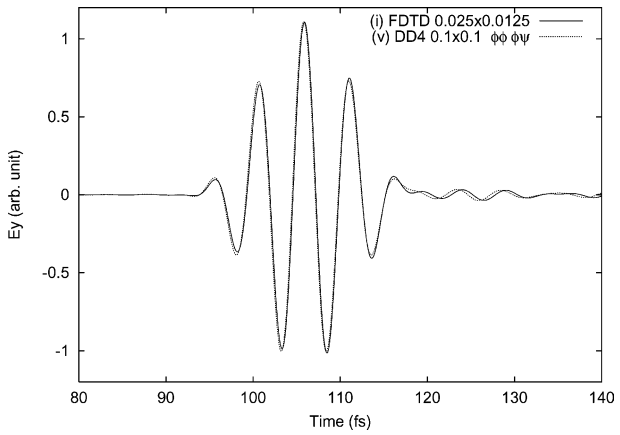

Fig. 9. Comparison of the time series data V_2 between FDTD and DD_4.

It has been found in the numerical dispersion analysis [17] that the scheme based on the scaling functions has one physical branch in the ωk-diagram and is unconditionally stable. However, the scheme that includes the wavelet terms has two branches, namely a physical mode and a spurious mode. The spurious mode may cause numerical instability, which results in an unbounded exponential increase in the magnitude of the time signal, called the 'late-time instability.' This is similar to the situation in the FDTD subgridding technique. However, for the waveguide analysis in this section, no instability was observed for 30,000 time steps even if the wavelet $\phi(x)\psi(z)$ was added to the core region; the stable duration could have been stretched for more time steps.

A series of numerical tests has shown that the instability is not observed in the analysis of open structures that are surrounded by absorbing boundaries, which are the main application of interest in this paper. The present scheme becomes unstable if we analyze sharp resonant structures that contain steep interface of dielectric media with their interface perpendicular to the axis of the wavelet involved. If the dielectric interface is parellel to the axis of the wavelets, then the scheme is stable. This is considered to be reasonable because the absorbing boundaries prevent the numerical errors from accumulating in the analysis region. Since the time-evolution methods sometimes suffer from the late-time instability due to the accumulation of numerical errors, it is a useful technique to introduce a slight dissipation in the system to suppress the energy of the spurious mode; the absorbing boundary in the present method plays an equivalent role without introducing losses that may affect the analysis results.

3.2. Analysis of waveguide beam splitter

A waveguide beam splitter shown in Fig. 10 has been analyzed with the proposed method and the standard FDTD. The configuration is more computationally extensive than the waveguide analyzed in Section 3.1, thus DD_{10} has been chosen as the basis, which is expected to allow coarser cells than that of DD_4. The beam splitter consists of four waveguide branches, which support up to a few higher-order modes, crossing at the center mirror section. The refractive indices for the clad (air), core and the mirror regions are $n_1 = 1.0$, $n_2 = 3.0$ and $n_3 = 2.0$, respectively. The width and the length of all the waveguide branches are respectively 2 μm and 8 μm, resulting in the whole analysis region of 18×18 μm^2, and the analysis region is surrounded by the 10-layer APML ABC. The center mirror was modeled by the stair case approximation with the average thickness of $d = 0.5$ μm.

Three different resolutions were investigated as summarized in Table 7. The structure was modeled first with FDTD (i), and then with the proposed method using the DD_{10} scaling function only (ii), and finally

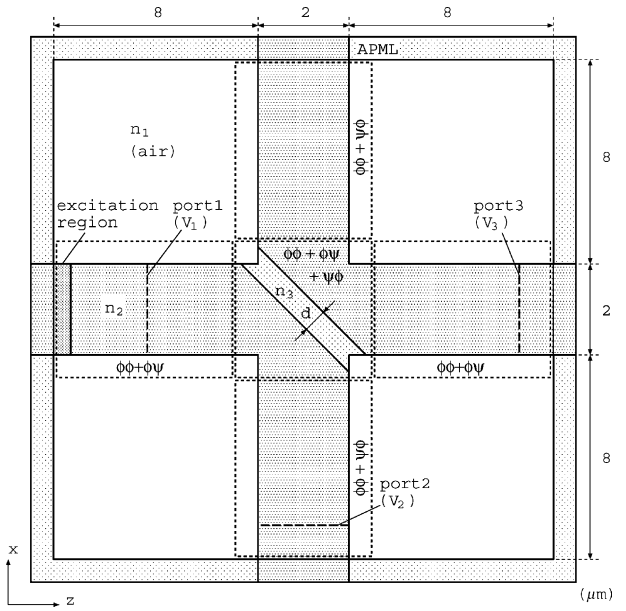

Fig. 10. Waveguide beam splitter configuration. Refractive indexes are $n_1 = 1.0$, $n_2 = 3.0$ and $n_3 = 2.0$. The thickness of the center mirror is $d = 0.5$ μm.

Table 7
Analysis conditions for the waveguide beam splitter of Fig. 10

	Scheme	Δx (μm)	Δz (μm)	Time steps	CPU time	Memory (MBytes)
(i)	FDTD	0.0125	0.0125	10176	81m44s	234
(ii)	DD_{10}, $\phi\phi$ only	0.05	0.05	12719	16m16s	37
(iii)	DD_{10}, $\phi\phi$ $\phi\psi$ and $\psi\phi$	0.1	0.1	6360	3m27s	31

with the DD_{10} scaling function and the wavelets (iii). In (iii), the wavelet term $\phi(x)\psi(z)$ or $\psi(x)\phi(z)$ was applied in the direction of wave propagation for 1.2 times wider regions covering each core region; and at the center mirror section, both $\phi(x)\psi(z)$ and $\psi(x)\phi(z)$ were applied with the inhomogeneity correction terms. Preliminary experiments showed that, in the center region, the wavelet coefficients associated with $\psi(x)\psi(z)$ was in the order of 10^{-5} in magnitude and did not significantly improve the accuracy, while the CPU time increased by 40%.

The excitation pulse of the time function as in the previous section, of which center frequency was again 193 THz ($\lambda = 1.55$ μm), was launched at the end of the left branch with the TE_0 mode distribution, and the time signals were detected at ports 1 and 2 by integrating E_y over the transversal cross section of the core waveguide. Figs. 11 and 12 show the time signals detected at ports 1 and 2, respectively. The present scheme with DD_{10} wavelets (iii) resulted in a slightly smaller V_2 than that of other resolutions; this is due mainly to the relatively coarse cells and to the staircase approximation which may cause a modeling error of the center mirror. In Figs. 11 and 12, again no late-time instability was observed.

The computational requirement has been significantly reduced in the proposed method compared to that of the standard FDTD; as shown in Table 7, the CPU time and the memory requirement have been reduced in (ii) by factors of five and six, respectively, by using the scaling function only; they are further reduced in

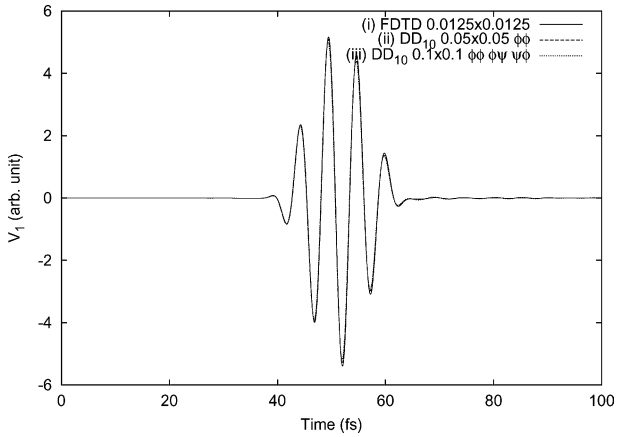

Fig. 11. Time series data of the beam splitter detected at port V_1.

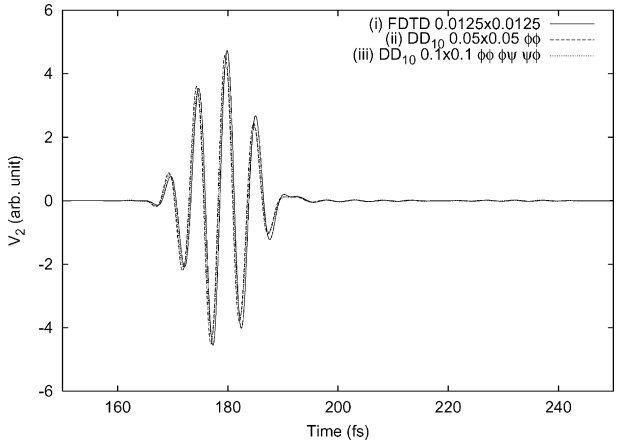

Fig. 12. Time series data of the beam splitter detected at port V_2.

(iii) by factors of 21 and seven, respectively, by adding the wavelet terms only where necessary. We performed the same analysis on a Sun workstation with 275 MHz clock rate and 256 Mbytes of RAM; for FDTD, the physical size of RAM was not enough and needed a swap memory, resulting in a excessive CPU time of over 9 h, while (iii) took 30 min. The proposed scheme can be straightforwardly extended to the three dimensions as in the usual finite difference scheme; one can further expect for three-dimensional cases the relative reduction of the computational expenditure compared to the standard FDTD.

4. Conclusion

The biorthogonal interpolating wavelets have been applied to the electromagnetic field analysis through the time-domain wavelet-collocation method. The algorithm has been applied to the analysis of two-dimensional dielectric waveguides that have a typical dimension of integrated planar optical waveguides.

The interpolating bases associated with their duals in the form of linear combination of Diracs yield schemes of arbitrary orders of regularity while saving the numerical overhead of the field reconstruction process. The proposed method has been found particularly efficient for the analysis of electrically large problems such as optical waveguides that have been difficult to solve with the conventional FDTD method due to the excessive computational expenditure.

The analyses of the simple waveguide structure by the present method have demonstrated that the reduction of the computational resources is typically one ninth of CPU time and one fifth of memory of those of the conventional FDTD, while maintaining the accuracy. Analyses of larger and more complicated structures have extended the computational efficiency further, achieving typically one twentieth of CPU time and one seventh of memory requirement compared to the standard FDTD. Higher relative efficiency compared to the FDTD is expected for three-dimensional full-wave analyses.

References

[1] A. Harten, Adaptive multiresolution schemes for shock computations, J. Comput. Phys. 115 (1994) 319–338.
[2] D.L. Donoho, Interpolating wavelet transforms, Technical Report, Department Statistics, Stanford University, Stanford, CA, 1992, preprint.
[3] D. Schulz, C. Glingener, E. Voges, Novel generalized finite-difference beam propagation method, IEEE J. Quantum Electron. 30 (4) (1994) 1132–1140.
[4] E. Bacry, S. Mallat, G. Papanicolaou, A wavelet based space–time adaptive numerical method for partial differential equations, Math. Model. Numer. Anal. 26 (1992).
[5] E.M. Tentzeris, R.L. Robertson, J.F. Harvey, L.P.B. Katehi, Stability and dispersion analysis of Battle–Lemarié-based MRTD schemes, IEEE Trans. Microwave Theory Tech. 47 (7) (1999) 1004–1013.
[6] G. Beylkin, On the representation of operators in bases of compactly supported wavelets, SIAM J. Numer. Anal. 6 (6) (1992) 1716–1740.
[7] G. Deslauriers, S. Dubuc, Symmetric iterative interpolation processes, Constr. Approx. 5 (1989) 49–68.
[8] I. Daubechies, Orthogonal bases of compactly supported wavelets, Comm. Pure Appl. Math. 41 (1988) 909–996.
[9] K.S. Yee, Numerical solution of initial boundary value problems involving Maxwell's equation in isotropic media, IEEE Trans. Antennas Propagation 14 (5) (1966) 302–307.
[10] L. Jameson, On the wavelet based differentiation matrix, J. Sci. Comput. 8 (1993) 267–305.
[11] M.D. Feit, J.A. Fleck Jr., Light propagation in graded index fibers, Appl. Opt. 24 (1978) 3390–3998.
[12] M. Fujii, W.J.R. Hoefer, Dispersion of time domain wavelet-Galerkin method based on Daubechies' compactly supported scaling functions with three and four vanishing moments, IEEE Microwave Guided Wave Lett. 10 (4) (2000) 125–127.
[13] M. Fujii, W.J.R. Hoefer, Application of biorthogonal interpolating wavelets to the Galerkin scheme of time dependent Maxwell's equations, IEEE Microwave Wireless Components Lett. 11 (1) (2001) 22–24.
[14] M. Fujii, W.J.R. Hoefer, Time-domain wavelet-Galerkin modeling of two-dimensional electrically large dielectric waveguides, IEEE Trans. Microwave Theory Tech. 49 (5) (2001) 886–892.
[15] M. Fujii, W.J.R. Hoefer, A wavelet formulation of finite difference method: full vector analysis of optical waveguide junctions, IEEE J. Quantum Electron. 37 (8) (2001) 1015–1029.
[16] M. Holmström, Solving hyperbolic PDEs using interpolating wavelets, SIAM J. Sci. Comput. 21 (2) (1999) 405–420.
[17] M. Krumpholz, L.P.B. Katehi, MRTD: new time-domain schemes based on multiresolution analysis, IEEE Trans. Microwave Theory Tech. 44 (4) (1996) 555–571.
[18] O.V. Vasilyev, C. Bowman, Second-generation wavelet collocation method for the solution of partial differential equations, J. Comput. Phys. 165 (2000) 660–693.
[19] O.V. Vasilyev, S. Paolucci, M. Sen, A multilevel wavelet collocation method for solving partial differential equations in a finite domain, J. Comput. Phys. 120 (1995) 33–47.
[20] R. Robertson, E. Tentzeris, M. Krumpholz, L.P.B. Katehi, Modeling of dielectric cavity structures using multiresolution time-domain analysis, Int. J. Numer. Model. 11 (1998) 55–68.
[21] S. Bertoluzza, G. Naldi, J.C. Ravel, Wavelet methods for the numerical solution of boundary value problems on the interval, in: C.K. Chui, L. Montefusco, L. Puccio (Eds.), Wavelets: Theory Algorithms and Applications, Academic Press, New York, 1994, pp. 425–448.
[22] S.D. Gedney, An anisotropic perfectly matched layer absorbing media for the truncation of FDTD lattices, IEEE Trans. Antennas Propagation 44 (12) (1996) 1630–1639.

[23] S. Dubuc, Interpolation through an iterative scheme, J. Math. Anal. Appl. 114 (1986) 185–204.
[24] S.G. Mallat, A Wavelet Tour of Signal Processing, Academic Press, San Diego, CA, 1997.
[25] S. Qian, J. Weiss, Wavelets and the numerical solution of partial differential equations, J. Comput. Phys. 106 (1993) 155–175.
[26] W. Sweldens, The lifting scheme: a construction of second generation wavelets, SIAM J. Math. Anal. 29 (2) (1997) 511–546.
[27] W. Sweldens, R. Piessens, Wavelet sampling techniques, in: 1993 Proceedings of the Statistical Computing Section, American Statistical Association, 1993, pp. 20–29.
[28] Y.W. Cheong, Y.M. Lee, K.H. Ra, J.G. Kang, C.C. Shin, Wavelet-Galerkin scheme of time-dependent inhomogeneous electromagnetic problems, IEEE Microwave Guided Wave Lett. 9 (8) (1999) 297–299.